IDENTIFYING GALAXY MERGERS IN HIGH REDSHIFT CLUSTERS USING THE HUBBLE SPACE TELESCOPE

An Undergraduate Research Scholars Thesis

by

COURTNEY WATSON

Submitted to the Undergraduate Research Scholars program
Texas A&M University
in partial fulfillment of the requirements for the designation as an

UNDERGRADUATE RESEARCH SCHOLAR

Approved by Research Advisor: Dr. Kim-Vy Tran

May 2017

Major: Physics and Astronomy

ABSTRACT

Identifying Galaxy Mergers In High Redshift Clusters Using The Hubble Space Telescope

Courtney Watson
Department of Physics and Astronomy
Texas A&M University

Research Advisor: Dr. Kim-Vy Tran
Department of Physics and Astronomy
Texas A&M University

We propose a photometric and spectroscopic study of merging galaxies within two recently discovered high redshift clusters at $z \sim 1.6$ and $z \sim 2.0$. We use imaging taken with the Hubble Space Telescope's (HST) Wide Field Camera-3 (WFC3) in three filters: F105W, F125W, and F160W. Spectral data will be obtained from the 3D-HST survey taken with the WFC3 in two grisms: G102 in Field A and G141 in Field B. By combining our photometric measurements with the 3D-HST observations, we present a complete survey of potentially merging objects in two high redshift clusters.

DEDICATION

To my mother, my father, and The Gang

ACKNOWLEDGMENTS

I would like to thank my research advisor Dr. Kim-Vy Tran for her guidance and support throughout the course of this research. Thanks also go to graduate students Leo Alcorn and Ben Forrest for their help and putting up with my incessant questioning. I would like to extend my gratitude to the National Science Foundation, whose generous grant allowed me to conduct my research.

Finally, thanks to my mother and father for their encouragement and support.

NOMENCLATURE

HST	Hubble Space Telescope
WFC3	Wide Field Camera-3
PSF	Point Spread Function
STSDAS	Space Telescope Science Data Analysis System
NCS	New Firm Cluster Survey
WCS	World Coordinate System

TABLE OF CONTENTS

Page

ABSTRACT ii

DEDICATION iii

ACKNOWLEDGMENTS iv

NOMENCLATURE v

TABLE OF CONTENTS vi

LIST OF FIGURES viii

LIST OF TABLES x

1. INTRODUCTION 1

2. METHODOLOGY 3

2.1 Data Sources 3
2.1.1 HST Observations 3
2.1.2 Grism Observations 4
2.2 Data Reduction 5
2.2.1 HST Image Analysis 5
2.2.2 Catalog Creation 6
2.2.3 Grism Analysis 8

3. RESULTS 10

3.1 Combining Photometry and Spectroscopy 10
3.1.1 Quality and Consistency Tests 11
3.2 Galaxy Mergers 11

4. SUMMARY AND CONCLUSIONS 17

REFERENCES 18

APPENDICES 19
A. Extra Figures 19

B. Data Tables 22

LIST OF FIGURES

FIGURE Page

2.1 RGB composite mosaics for *Left*: Field A: IRC0222A ($1.0 < z < 1.9$); *Right*: Field B: IRC0222B ($1.6 < z < 2.4$). Both fields measure 2432×2154 pixels or $146" \times 129"$. 3

2.2 The full interlaced grism image for *Left*: Field A: IRC0222A ($1.0 < z < 1.9$); *Right*: Field B: IRC0222B ($1.6 < z < 2.4$). Both fields measure $2488 \times 2092\ pixels$. 4

2.3 Example curve of growth for Field A using the flux measured in the F160W filter from SExtractor. We see that the amount of fluxed enclosed within apertures of various size begin to level off around 1 arcsec 7

2.4 Sample of the spectral fits provided by the 3D-HST survey used to determine wether the redshift measurements are reliable. *Top row*: IRC0222A object ID: 292 (Grism), 2102 (NCS). *Bottom row*: IRC0222B object ID 65 (Grism), 7388 (NCS). Starting from the left, *First Panel*: calibrated flux. *Second panel*: applied flux corrections. *Third Panel*: probability chart of redshift with the spectroscopic redshift (z_{grism}) indicated by the peak in the green curve and the photometric redshift (z_{phot}) represented with the blue. *Last Panel*: galaxy energy distribution where the model is indicated in blue 9

3.1 Comparison between photometric and spectroscopic redshifts in Field A(*left*) and Field B (*right*). *Top:* spectroscopic vs. photometric redshift for each object in the master catalog. *Bottom:* $\Delta z/(1+z)$ as a function of spectroscopic redshift. Points are colored based on their redshift quality flag (Q_z) value. Filled points indicate objects whose data quality (DQ) was flagged as 1 or "good" while unfilled points are objects whose DQ was flagged as 0 or "bad." The dashed lines in the lower panel indicate $\pm 2\sigma_{NMAD}$. 10

3.2 Histograms of Field A (*left*) and Field B (*right*) showing the distribution of grism redshifts within the whole field (top), and within the projected redshift range of the cluster (A: [1.55-1.9] ; B: [1.8-2.2]), indicated by the black dashed lines (bottom). Objects in the field that have been identified as possible mergers are shown in the hatched regions. . . 12

3.3 Color Magnitude Diagram of Field A (*left*) and Field B (*right*) showing all the objects detected in SExtractor, as well as objects included in the master catalog. Objects identified as stars or potentially merging are also indicated. 13

3.4 Thumbnails of the visually identified merger candidates who lie within the proposed redshift range ($z = 1.55 - 1.9$) of the cluster in IRC0222A. Each thumbnail lists the objects' photometric and grism redshifts, their data quality (DQ) and redshift quality (Q_z) flags, and the pair's F160W flux ratio. 14

3.5 Thumbnails of the visually identified merger candidates who lie within the proposed redshift range ($z = 1.8 - 2.2$) of the cluster in IRC0222B. Each thumbnail lists the objects' photometric and grism redshifts, their data quality (DQ) and redshift quality (Q_z) flags, and the pair's F160W flux ratio. 15

3.6 Sample spec image of one merger candidate located in IRC0222A showing (from top to bottom) the thumbnail image (*first*) and the 2D and 1D spectra (*second and third, fourth and fifth*) for each object in the merger. 16

1 Thumbnails of all the visually identified merger candidates throughout all of Field A. Each thumbnail lists the objects' photometric and grism redshifts, their data quality (DQ) and redshift quality (Q_z) flags, and the pair's F160W flux ratio. 21

LIST OF TABLES

TABLE		Page
1	Thumbnails of all the visually identified merger candidates throughout all of Field B. Each thumbnail lists the objects' photometric and grism redshifts, their data quality (DQ) and redshift quality (Q_z) flags, and the pair's F160W flux ratio.	19
2	WFC3 Filter Information	22
3	IRC0222A Merger Photometry	23
4	IRC0222A Merger Coordinate Data. NCS RA and Dec coordinates are ground-based.	24
5	IRC0222B Merger Photometry	25
6	IRC0222B Merger Coordinate Data	28

1. INTRODUCTION

Our current model of formation and evolution utilizes hierarchal merging, a process in which numerous small structures merge to form larger objects, which then merge to form even bigger objects. This progression continues until the massive galaxies seen in our current epoch emerge. This process is considered to be one of the most important mechanisms in the formation of structure throughout the Universe. Because evidence of minor merging events among these massive objects and some of their satellite galaxies still exists today, we assume this process must have been even more prevalent in the early universe. The easiest method for investigating this phenomenon involves examining galaxies within clusters. Galaxies are typically found in groups or clusters comprised of anywhere between fewer than 50 and more than hundreds of thousands of gravitationally bound objects. Studying these clusters at redshifts between 1-3 proves particularly useful, because they provide a rather large sample of similarly ages objects at the peak of their star formation. Examining galaxies in this way enables the measurement of their various characteristics. By comparing these measurements with those of the local universe, we can build a clearer picture of how galaxies evolve. This also offers insights into how galaxies interact with each other and their environment within the cluster. Unfortunately, few studies have been conducted on the merger process in high redshift clusters due to a previous lack of imaging with enough resolution to distinguish individual objects within a merger process at high redshifts. For our study on the properties of merging galaxies we refer to Tran et al. (2008), van Dokkum et al. (1999), and Schmidt et al. (2013).

We refer to studies done by Williams et al. (2011) and Lotz et al. (2013) for our analysis of the merger fractions in each clusters. All of these works focus on identifying and analyzing merging galaxies at redshifts greater than $z \sim 1$. Out of all the studies refer-

enced, it should be noted only two or three use both photometric and spectroscopic data. In particular, when focusing in on the merger fraction, no studies have been conducted involving the use of both photometric and spectroscopic data sets; they generally resort to using one or the other and rely on simulated data to substitute for the missing set.

2. METHODOLOGY

2.1 Data Sources

We acquired two infrared fields of view from the Hubble Space Telescope (HST) Wide Field Camera-3 (WFC3) as well as grism observations for the performance of our various extraction procedures and data analysis. The following describes both of these data sets.

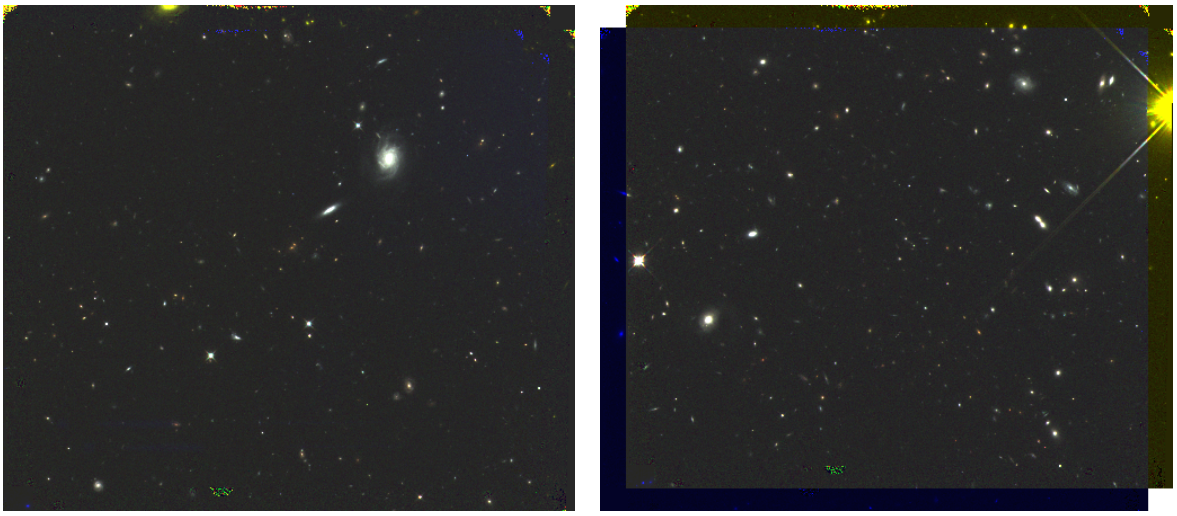

Figure 2.1: RGB composite mosaics for *Left*: Field A: IRC0222A ($1.0 < z < 1.9$); *Right*: Field B: IRC0222B ($1.6 < z < 2.4$). Both fields measure 2432×2154 pixels or $146" \times 129"$.

2.1.1 HST Observations

Our image data was obtained by the 3D-HST Treasury Survey (van Dokkum et al. (2011), Brammer et al. (2012), Skelton et al. (2014)). All near-infrared HST observations were obtained using the WFC3 IR detector in the Hubble telescope. The observations used were done in three wide filters: F105W, F125W, and F160W, which cover the wavelength

ranges of $\sim$ $1.1\mu m$ - $1.4\mu m$, $\sim$ $1.2\mu m$ - $1.6\mu m$, and $\sim$ $1.4\mu m$ - $1.7\mu m$, respectively. Momcheva et al. (2015) and Brammer et al. (2012) present more detailed descriptions of these observations. We worked with two cluster candidates: IRC0222A ($1.0 < z < 1.9$), referred to as Field A, and IRC0222B ($1.6 < z < 2.4$), referred to as Field B (see Fig. 2.1).

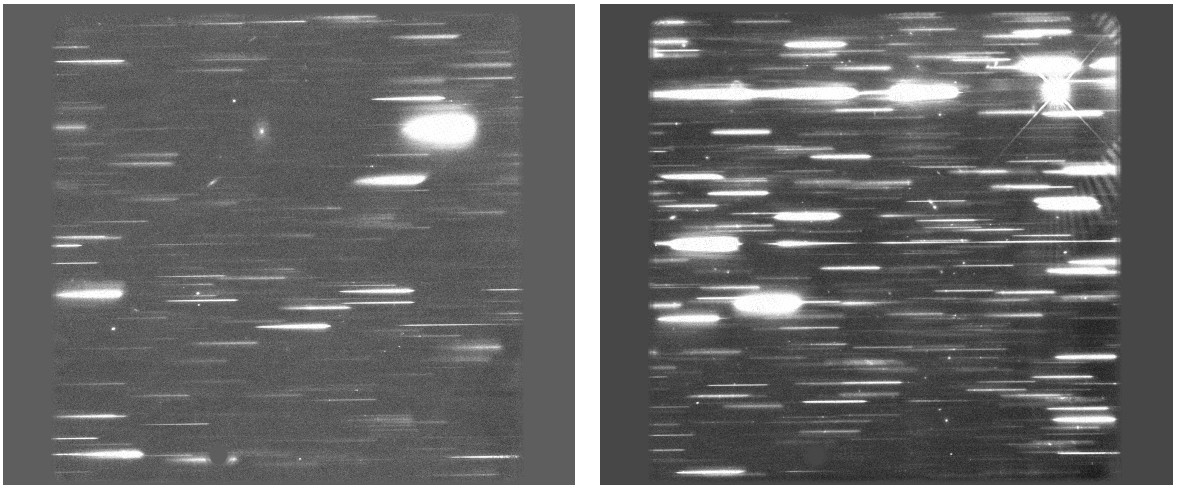

Figure 2.2: The full interlaced grism image for *Left*: Field A: IRC0222A ($1.0 < z < 1.9$); *Right*: Field B: IRC0222B ($1.6 < z < 2.4$). Both fields measure 2488×2092 $pixels$.

2.1.2 Grism Observations

We obtained spectroscopic data from 3D-HST, which was already reduced. For information on the reduction process, refer to Momcheva et al. (2015). The images were taken with grisms equipped on the WFC3 camera (Fig. 2.2). Grisms are placed in the path of incoming light in lieu of a filter, acting like a prism to separate individual wavelengths. They are especially efficient in providing the spectra of all objects in the imaging field simultaneously.

For our data, which was imaged at near IR wavelengths, the G102 grism, with a F105W direct image, was used for Field A, while the G141, with a F140W direct image, was used for Field B. The G102 grism covers a wavelength range of 800-1150nm with a dispersion of 2.45nm/pixel. The G141 grism covers a range of 1075-1700nm, with a dispersion of 4.65nm/pixel. The wavelength ranges of both grisms enable us to see emissions of Hα, Hβ, O[III], and O[II], elements essential in the galaxy formation process. Momcheva et al. (2015) contains more information about the grism data.

2.2 Data Reduction

We performed two types of analysis on the datasets: a photometric analysis on the HST images and a spectroscopic analysis on the grism data. This section describes further details of these processes. For the majority of our reduction and analysis, we use coding routines contained within the STSDAS PyRAF package.

2.2.1 HST Image Analysis

We modeled the photometric analysis of the HST images on certain analysis techniques found in Skelton et al. (2014). We downloaded the calibrated images and association tables from the MAST archive, which were processed by the calwfc3 pipeline. A number of corrections were applied to improve the data's quality and produce the final data products: masking satellite trails, persistence correction, sky-subtraction, flat-field re-application, initial astrometric alignment, and additional cosmic ray and bad pixel rejection.

We began with Astrodrizzle, using the default parameters and changing the bit value to 8192, final_wht_type=IVM, and final_pixfrac=0.8 (Skelton et al. (2014)), with an initial run to remove cosmic rays and bad pixels. This allowed for improved alignment within Tweakreg. The initial drizzling also enabled the use of the F160W image as a reference image to improve alignment in Tweakreg. The initial run produced "crclean" images, indicating they were then free of most of their cosmic rays. After the cosmic rays were

removed, we used Tweakreg to align all crclean images within a given filter to a common World Coordinate System (WCS) and used the F160W image as a reference for alignment. This means when we ran Tweakreg on the F125W and F140W filters, they both were aligned according to the WCS information contained in the header of the F160W image, ensuring actual pixel alignment in the final drizzled product. When we were satisfied with the alignment, the headers of all the crclean images are updated with the new coordinate information. Once the crclean images were updated, we propagated the new coordinate information back to the original *_flt.fits* images. This was accomplished using Tweakback, which sends the updated crclean header information back to the original, untouched, *_flt.fits* images. Using the newly updated *_flt.fits* images, we reran Astrodrizzle to drizzle and combine all the images within each filter. For this final run, we used the same parameters described earlier with the addition of final_scale=0.06. This set the pixel scale of each image to $0.06"/pixel$. The resulting three combined and aligned mosaics within the F125W, F140W, and F160W filters comprised an area of $2432 \times 2154\ pixels$ or $146" \times 129"$ (Fig. 2.1).

2.2.2 Catalog Creation

We used the data taken from HST and a program called Source Extractor (SExtractor) (Bertin & Arnouts (1996)) to analyze the photometry of the fields. We implemented this step after analyzing the images using DrizzlePac as we had highlighted. For SExtractor, we created a stacked image of the F125W and F160W images to use as detection image. This was done to make sure all possible objects found within both the F125W and F160W images are used as detectable objects in SExtractor, since the two filters actually cover slightly different areas in the sky. The F105W image was omitted in this stacked image due to excessive artifacts, which generated too much noise, and its interference with SExtractor's measurements. Each filter's drizzled image was ran using dual-image mode

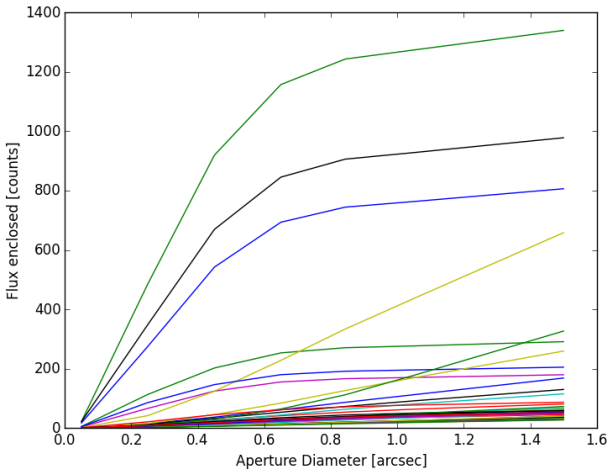

Figure 2.3: Example curve of growth for Field A using the flux measured in the F160W filter from SExtractor. We see that the amount of fluxed enclosed within apertures of various size begin to level off around 1 arcsec

against the stacked image for measurements. We used 7 different sized apertures ranging from $0.83 - 25\ pixels$, or $0.05" - 1.5"$, to measure fluxes and magnitudes. The AB magnitude zeropoint, and gain were set for each filter. The HST website provided the AB zeropoint for each filter, and the header information from each image provided the gain. The final images had a pixel scale of 0.06"/pixel to obtain the best possible resolution without interfering with photometry measurements.

We used Source Extractor's ability to generate check images to confirm the software's identification of all objects. We used a segmentation map to visually separate each identified source from our SExtractor run. We also used the aperture image to visualize the number of apertures for each object and determine their proper size. With the fluxes and magnitudes from these apertures, we created curves of growth (COGs) (see Fig. 2.3) for each filter representing the change in the amount of flux of each object with growing aperture size . We used these COGs to verify the similarity of the Point Spread Functions

(PSFs) of each filter. This remains an important step when combining ground-based data with space-based data, ensuring our measurements are accurate and reliable.

2.2.3 Grism Analysis

As previously described, our spectroscopic data was already reduced, meaning they had been previously drizzled and aligned. The grism data was comprised of 1D and 2D FITS files as well as model data to which the grism objects had already been compared for accuracy. The 1D file contains a 1D representation of the grism object, with the measured fluxes and wavelengths organized into an easily accessible table. The 2D file contains a stack of images comprising a thumbnail of the object, the associated 2D spectra, the contamination model, and the grism-contamination subtracted spectra. Grism redshifts were obtained by measurement of the emission lines present in each object spectra.

We began the analysis with visual inspections of each grism image. The first goal of the visual inspections was to identify any problems in the data's quality. The secondary goal of the inspections was to assign flags for both the data's quality and the redshift's reliability. The data quality (DQ) flags were used to note whether the spectra was affected by known failure modes. Common failures that affect the data's quality include: incomplete masking of 0th-order spectra which can mimic emission lines (that overlap mentioned earlier), residuals from the spectra of very bright stars which may not be subtracted properly, and instances where corrupted photometric measurements lead to errors in the spectral fit. The inspection's primary criterion was whether the redshift was clearly affected by the error in the spectrum or not. For example, objects located at the edge of the field generally have incomplete spectra. These were flagged as "bad" in quality with a DQ of 0. Individual DQ classifications were either "good" or "bad". Redshift quality (Q_z) flags are assigned based on visual inspections of the 1D and 2D spectra, comparison to the model data (Fig. 2.4), as well as the photometric redshift data. The Q_z flags are an

indicator of whether or not the grism measurements are reliable. Objects flagged with a redshift quality (Q_z) of 3 indicate a robust grism measurement, while those with Q_z of 2 are less robust, but still reliable. In most of the figures presented here, we show only those objects whose data quality was flagged as good, i.e. little to no contamination, and whose redshift quality was flagged as "robust" or "good."

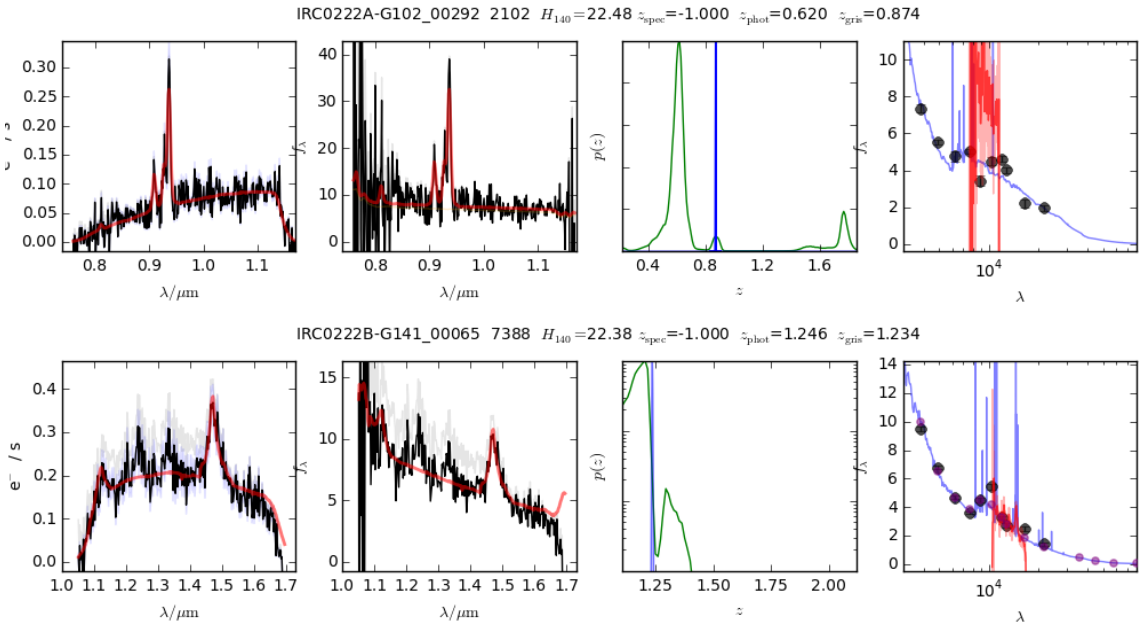

Figure 2.4: Sample of the spectral fits provided by the 3D-HST survey used to determine wether the redshift measurements are reliable. *Top row*: IRC0222A object ID: 292 (Grism), 2102 (NCS). *Bottom row*: IRC0222B object ID 65 (Grism), 7388 (NCS). Starting from the left, *First Panel*: calibrated flux. *Second panel*: applied flux corrections. *Third Panel*: probability chart of redshift with the spectroscopic redshift (z_{grism}) indicated by the peak in the green curve and the photometric redshift (z_{phot}) represented with the blue. *Last Panel*: galaxy energy distribution where the model is indicated in blue

3. RESULTS

3.1 Combining Photometry and Spectroscopy

We obtained photometric redshifts from a catalogue previously generated by a ground-based spectroscopic survey (NCS) and used them for comparison of our space-based data. The ground-based NCS catalog easily joined with the data obtained by the grism images based on object ID number. These objects were then matched, based on the object's coordinates, to objects detected in the SExtractor catalogs to create master catalogs for each field. In this study, we used the photometric redshift from the NCS data, the spectroscopic redshift from the grism data, and the flux and magnitude recorded in the SExtractor catalogs.

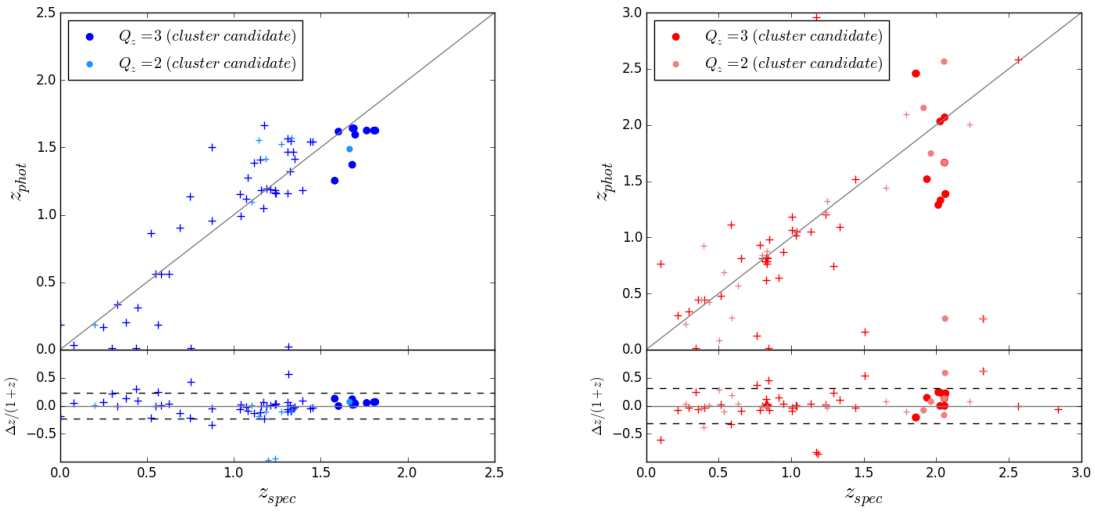

Figure 3.1: Comparison between photometric and spectroscopic redshifts in Field A(*left*) and Field B (*right*). *Top:* spectroscopic vs. photometric redshift for each object in the master catalog. *Bottom:* $\Delta z/(1+z)$ as a function of spectroscopic redshift. Points are colored based on their redshift quality flag (Q_z) value. Filled points indicate objects whose data quality (DQ) was flagged as 1 or "good" while unfilled points are objects whose DQ was flagged as 0 or "bad." The dashed lines in the lower panel indicate $\pm 2\sigma_{NMAD}$.

3.1.1 Quality and Consistency Tests

To determine the accuracy of the grism redshifts, we created a plot to compare them against the available ground-based data. Figure 3.1 shows the comparison of spectroscopic to photometric redshift for each field.

To verify the reliability of our measurements, we calculate the NMAD scatter as:

$$\sigma_{NMAD} = median(|\Delta z - median(\Delta z)|) \times 1.48 \tag{3.1}$$

where

$$\Delta z = \frac{z_{spec} - z_{phot}}{1 + z_{spec}} \tag{3.2}$$

While initially the NMAD scatter (σ_{NMAD}) of each data set seem high (σ_{NMAD}= 0.122 and σ_{NMAD}= 0.179 for Fields A and B, respectively), the NMAD scatter was reducted to σ_{NMAD}= 0.078 and σ_{NMAD}= 0.119 for A and B, respectively, when outliers with deviations greater than 2σ were removed.

Figure 3.2, shows the distribution of spectroscopic redshifts within each field. These show that the cluster in Field A is at a redshift of $z \sim 1.3$ while Field B may house two clusters at redshifts $z \sim 0.9$ and $z \sim 2.1$.

We generated color magnitude diagrams (see Fig. 3.3) in order to assess the objects' colors. We use the F160W filter, which measures the longest wavelength, as a base to show the other filters' wavelength deviation and the objects' redness. To determine the object's color, we used the difference in the magnitude detected in the F125W images and the F160W images.

3.2 Galaxy Mergers

To select the merger candidates later used for a ground-based observation run, we used a visual identification technique that consisting of layering all three filters to create

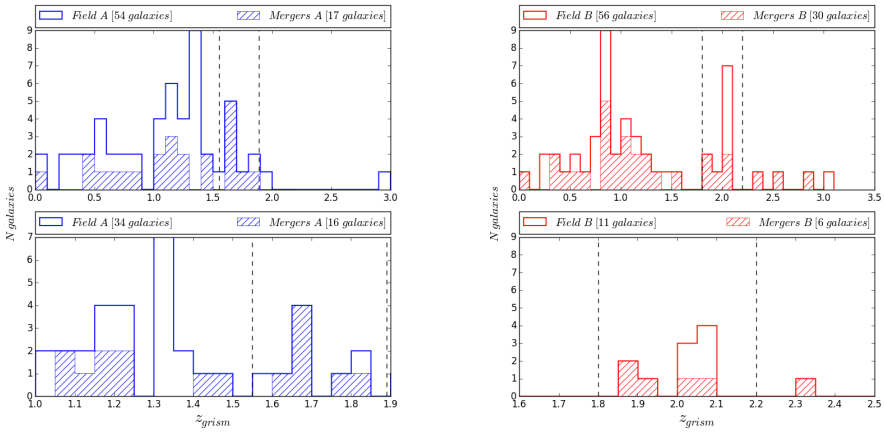

Figure 3.2: Histograms of Field A (*left*) and Field B (*right*) showing the distribution of grism redshifts within the whole field (top), and within the projected redshift range of the cluster (A: [1.55-1.9] ; B: [1.8-2.2]), indicated by the black dashed lines (bottom). Objects in the field that have been identified as possible mergers are shown in the hatched regions.

an RGB (red-green-blue) image (see Fig.2.1) in DS9 and then carefully picked a pair of neighboring galaxies, which fit in a 3" diameter. This means any object found to be within 3" of another object was flagged as a merger candidate. These galaxies were good candidates for potential gravitational attracted galaxies. For Field A, 60 possible mergers were identified visually and 33 of these had recorded spectroscopic redshifts. For Field B, there were 104 possible mergers identified, of which 64 had recorded spectroscopic redshifts. Thumbnail images of some of the merger candidates for Field A and Field B are shown in Figures 3.4 and 3.5. Full image arrays of the merger candidates can be found in the appendix. Using these thumbnail images together with the 1D and 2D grism spectra from 3D-HST, we created spec images for each of the merger candidates (an example is shown in Fig. 3.6) which show the spectra for each proposed merger pair.

According to the color magnitude diagrams in Figure 3.3, most candidate galaxies have a brighter F160W magnitude and a relatively low difference between the F160W and F125W filters, indicating these objects were more red in color. From the redshift

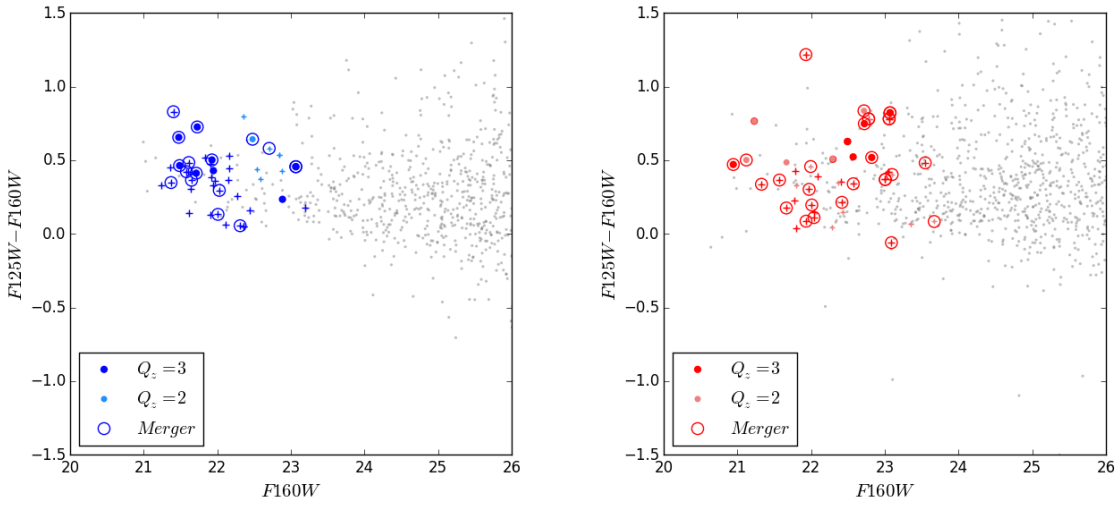

Figure 3.3: Color Magnitude Diagram of Field A (*left*) and Field B (*right*) showing all the objects detected in SExtractor, as well as objects included in the master catalog. Objects identified as stars or potentially merging are also indicated.

distributions shown in Figure 3.2, we see a small fraction of the merger candidates in Field B lie in the proposed redshift range of the cluster. Field A shows a higher fraction of merger candidates lying in the proposed redshift range of the cluster. Of the objects located within the projected redshift range of IRC0222A (1.55< z <1.9), about 77% are possible merger candidates. Of the objects found in the projected redshift range of IRC0222B (1.8< z <2.2), only 50% are possible merger candidates.

Figure 3.4: Thumbnails of the visually identified merger candidates who lie within the proposed redshift range ($z = 1.55 - 1.9$) of the cluster in IRC0222A. Each thumbnail lists the objects' photometric and grism redshifts, their data quality (DQ) and redshift quality (Q_z) flags, and the pair's F160W flux ratio.

Figure 3.5: Thumbnails of the visually identified merger candidates who lie within the proposed redshift range ($z = 1.8 - 2.2$) of the cluster in IRC0222B. Each thumbnail lists the objects' photometric and grism redshifts, their data quality (DQ) and redshift quality (Q_z) flags, and the pair's F160W flux ratio.

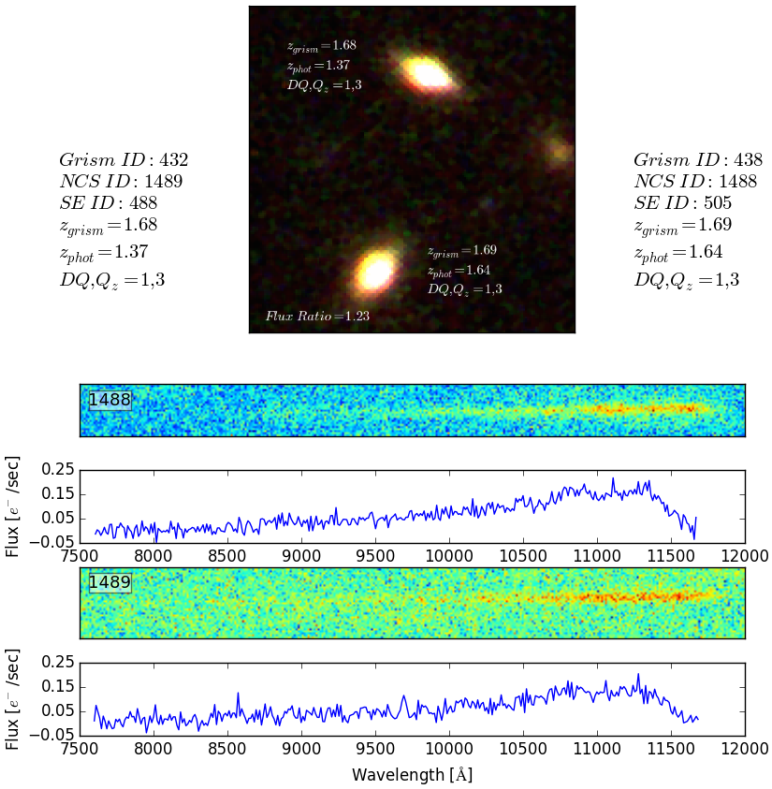

Figure 3.6: Sample spec image of one merger candidate located in IRC0222A showing (from top to bottom) the thumbnail image (*first*) and the 2D and 1D spectra (*second and third, fourth and fifth*) for each object in the merger.

4. SUMMARY AND CONCLUSIONS

Deep field imaging from the Hubble Space Telescope enabled us to see galaxies so distant, they appeared as nearly undetectable, dim dots in the color images. However, the high resolution of the HST images, allowed us to measure even the tiniest, dimmest galaxy in the field. Using these images we were able to use photometry to measure the fluxes - a measure of how much light an object is emitting - and magnitudes - how bright an object is - of all the galaxies within our two fields of view. We then used spectroscopy redshift measurements to determine whether proximal galaxies were actually "neighbors" in three dimensional space. This was useful since, when looking at the two dimensional images (e.g., Figure 2.1), two galaxies can appear to be located near each other, however, when measuring the redshifts, we often found they are actually separated by billions of light years. We then combined our photometric measurements with the redshifts obtained by spectroscopy to determine whether two or more galaxies, which appeared to be "neighbors" in the 2D images, could be identified a potential merger.

Our current model of galaxy formation depends upon the concept of galaxies growing through merging. This means we should observe higher merger fractions at greater redshifts (i.e. galaxies far far away). However, our data disagrees with this assertion. We actually observed a lower merger fraction in IRC022B (located at a higher redshift, $z \sim 1.8 - 2.2$) and a higher merger fraction in IRC0222A (located at a lower redshift, $z \sim 1.5 - 1.9$).

Our next steps will be measuring the star formation rates and stellar masses of each of the merger candidates, allowing us to build a clearer picture of these galaxies' characteristic. This will give us a better idea of how these galaxies are interacting with each other, as well as their environment within the cluster.

REFERENCES

Bertin, E., & Arnouts, S. 1996, Astronomy and Astrophysics Supplement Series, 117, 393

Brammer, G. B., van Dokkum, P. G., Franx, M., et al. 2012, The Astrophysical Journal Supplement Series, 200, 13

Lotz, J. M., Papovich, C., Faber, S. M., et al. 2013, The Astrophysical Journal, 773, 154

Momcheva, I. G., Brammer, G. B., van Dokkum, P. G., et al. 2015, arXiv.org, 1510, 2106

Schmidt, K. B., Rix, H. W., da Cunha, E., et al. 2013, Monthly Notices of the Royal Astronomical Society, 432, 285

Skelton, R. E., Whitaker, K. E., Momcheva, I. G., et al. 2014, The Astrophysical Journal Supplement Series, 214, 24

Tran, K.-V. H., Moustakas, J., Gonzalez, A. H., et al. 2008, 17

van Dokkum, P. G., Franx, M., Fabricant, D., Kelson, D. D., & Illingworth, G. D. 1999, The Astrophysical Journal, 520, L95

van Dokkum, P. G., Brammer, G., Fumagalli, M., et al. 2011, 1

Williams, R. J., Quadri, R. F., & Franx, M. 2011, The Astrophysical Journal, 738, L25

EXTRA FIGURES

Table 1: Thumbnails of all the visually identified merger candidates throughout all of Field B. Each thumbnail lists the objects' photometric and grism redshifts, their data quality (DQ) and redshift quality (Q_z) flags, and the pair's F160W flux ratio.

Continued on next page

Table 1 – continued from previous page

Figure 1: Thumbnails of all the visually identified merger candidates throughout all of Field A. Each thumbnail lists the objects' photometric and grism redshifts, their data quality (DQ) and redshift quality (Q_z) flags, and the pair's F160W flux ratio.

DATA TABLES

Table 2: WFC3 Filter Information

Filter	Wavelength Coverage (μm)	Gain	Exposure Time (sec)	Zeropoint (AB)
F105W	$1.1 - 1.4$	5433.76	2173.50	26.2687
F125W	$1.2 - 1.6$	3308.71	1323.49	26.2303
F160W	$1.4 - 1.7$	6558.78	2623.51	25.9463
G102	$0.8 - 1.15$	2224.2	889.68	26.2687
G141	$1.075 - 1.7$	1779.35	711.74	26.4524

Table 3: IRC0222A Merger Photometry

Grism ID	NCS ID	SE ID	Merger ID	z_{grism}	z_{phot}	F160W Flux	Merger Flux Ratio	F160W Magnitude
1078	1518	1263	2	0.750	1.136	70.4118	1.8105	21.3272
873	1258	1052	9	0.562	0.187	57.7408	1.2311	21.5426
853	1259	979	9	0.439	0.010	71.0859	1.2311	21.3168
797	2020	987	58	1.435	1.444	92.8846	1.0294	21.0264
785	2020	974	58	0.628	1.444	95.6152	1.0294	20.995
779	2118	1089	57	0.009	0.010	33.7339	13.2222	22.1261
613	1677	669	14	1.174	1.666	55.7462	7.9525	21.5808
587	1774	659	16	1.144	1.556	19.7788	2.1247	22.7058
584	1775	665	17	1.453	1.541	65.6058	1.9513	21.4039
575	1901	641	53	1.699	1.595	40.4926	13.6186	21.9279
557	1650	627	15	1.187	1.194	36.9344	5.2954	22.0277
533	1775	602	17	1.438	1.541	128.0177	1.9513	20.6781
470	1502	536	20	0.001	0.187	37.5484	3.3189	22.0098
439	1645	518	19	1.684	1.642	61.3530	1.2605	21.4767
438	1488	505	22	1.691	1.642	60.7358	1.2321	21.4877
436	1646	511	19	1.603	1.618	48.6748	1.2605	21.728
432	1489	488	22	1.682	1.372	49.2936	1.2321	21.7143
368	1478	428	23	1.667	1.488	24.3650	2.7515	22.4794
331	2273	386	48	1.072	1.117	67.5922	7.7453	21.3716
323	1779	355	25	0.444	0.315	188.5835	40.5265	20.2575
310	2274	348	48	1.236	1.168	54.1110	7.7453	21.6131
292	2102	342	46	0.874	1.503	28.4615	10.5381	22.3107
223	2265	271	45	2.158	1.060	21.5242	4.8842	22.614
183	1587	231	34	1.083	1.274	52.2874	0.1063	21.6503
100	2477	113	42	0.530	1.110	33.3405	0.38	22.1389
82	2079	34	38	1.210	1.188	88.4982	4.2161	21.079
49	1793	205	33	1.116	1.386	54.7921	6.7238	21.5995
19	1715	1	36	0.626	0.564	327.7356	38.6914	19.6575
685	1676	1234	5	1.815	1.626	14.1700	2.3148	23.0679
501	1502	578	20	0.199	0.187	11.5972	3.3189	23.2854
1057	1564	1289	1	0.104	0.198	67.2952	1.2697	21.3763
1036	1728	1290	60	1.122	1.155	40.9825	6.8678	21.9148
685	1676	1234	5	1.765	1.626	14.1700	2.3148	23.0679
501	1502	578	20	0.148	0.187	11.5972	3.3189	23.2854

Table 4: IRC0222A Merger Coordinate Data. NCS RA and Dec coordinates are ground-based.

Grism ID	NCS ID	SE ID	NCS RA	NCS DEC	HST RA	HST DEC	DQ	Q_z
1078	1518	1263	35.5014	-4.1941	35.5014	-4.1942	1	3
873	1258	1052	35.5187	-4.1852	35.5187	-4.1852	1	3
853	1259	979	35.5195	-4.1852	35.5195	-4.1851	1	3
797	2020	987	35.5001	-4.2097	35.4999	-4.2097	0	0
785	2020	974	35.5001	-4.2097	35.5002	-4.2097	0	0
779	2118	1089	35.5025	-4.2124	35.5024	-4.2124	0	0
613	1677	669	35.5153	-4.1987	35.5152	-4.1987	1	3
587	1774	659	35.5145	-4.2021	35.5145	-4.2020	1	2
584	1775	665	35.5136	-4.2027	35.5135	-4.2026	1	3
575	1901	641	35.5128	-4.2057	35.5127	-4.2057	1	3
557	1650	627	35.5182	-4.1977	35.5181	-4.1978	1	3
533	1775	602	35.5136	-4.2027	35.5137	-4.2026	1	3
470	1502	536	35.5243	-4.1928	35.5244	-4.1930	1	3
439	1645	518	35.5212	-4.1976	35.5211	-4.1976	1	3
438	1488	505	35.5255	-4.1925	35.5255	-4.1924	1	3
436	1646	511	35.5211	-4.1981	35.5210	-4.1981	1	3
432	1489	488	35.5261	-4.1931	35.5260	-4.1931	1	3
368	1478	428	35.5283	-4.1919	35.5283	-4.1920	1	2
331	2273	386	35.5131	-4.2174	35.5130	-4.2173	1	3
323	1779	355	35.5213	-4.2028	35.5212	-4.2028	1	3
310	2274	348	35.5132	-4.2178	35.5132	-4.2178	1	3
292	2102	342	35.5183	-4.2117	35.5183	-4.2117	1	3
223	2265	271	35.5176	-4.2169	35.5175	-4.2170	0	0
183	1587	231	35.5335	-4.1949	35.5334	-4.1948	1	3
100	2477	113	35.5178	-4.2239	35.5177	-4.2239	0	0
82	2079	34	35.5257	-4.2114	35.5256	-4.2113	1	3
49	1793	205	35.5288	-4.2027	35.5287	-4.2027	1	3
19	1715	1	35.5355	-4.2004	35.5354	-4.2004	1	3
685	1676	1234	35.5030	-4.1985	35.5028	-4.1984	1	3
501	1502	578	35.5243	-4.1928	35.5241	-4.1927	0	2
1057	1564	1289	35.4997	-4.1949	35.4998	-4.1948	0	0
1036	1728	1290	35.4950	-4.2007	35.4949	-4.2008	0	0
685	1676	1234	35.5030	-4.1985	35.5028	-4.1984	1	3
501	1502	578	35.5243	-4.1928	35.5241	-4.1927	1	1

Table 5: IRC0222B Merger Photometry

Grism ID	NCS ID	SE ID	Merger ID	z_{grism}	z_{phot}	F160W Flux	Merger Flux Ratio	F160W Magnitude
17	7368	1	56	0.675	0.541	424.3077	3.2528	19.3771
57	7342	30	59	1.936	1.518	17.7652	1.2001	22.8224
65	7388	3	58	1.235	1.201	37.4602	11.4123	22.0124
84	6826	75	42	1.037	1.048	38.8253	8.4341	21.9735
98	7392	92	57	2.860	3.838	39.8437	4.6662	21.9454
103	7367	112	56	0.525	0.202	130.4431	3.2528	20.6577
157	7259	159	50	0.342	0.010	51.6248	7.0677	21.6642
167	7306	171	51	2.058	2.069	19.4812	1.0044	22.7223
179	6546	189	32	0.849	0.982	13.8837	2.1439	23.09
185	7305	192	51	2.054	2.565	19.5677	1.0044	22.7175
185	7305	192	51	2.284	2.565	19.5677	1.0044	22.7175
187	6947	208	38	2.061	0.276	85.1185	2.2164	21.1212
206	6880	217	37	0.099	0.768	37.5566	2.6578	22.0096
217	6772	225	35	0.944	0.872	25.7836	2.6112	22.4179
223	6536	236	32	0.033	0.010	29.7654	2.1439	22.262
247	6841	253	36	1.335	1.091	49.3396	6.2532	21.7133
256	6694	267	34	2.100	3.626	17.9104	3.0603	22.8135
277	6866	292	37	1.858	2.459	14.1307	2.6578	23.0709
277	6866	292	37	1.862	2.459	14.1307	2.6578	23.0709

Continued on next page

Table 5 – continued from previous page

Grism ID	NCS ID	SE ID	Merger ID	z_{grism}	z_{phot}	F160W Flux	Merger Flux Ratio	F160W Magnitude
297	6712	318	33	2.564	2.586	40.4441	7.0650	21.9292
310	6974	327	41	2.329	0.276	18.4644	2.8272	22.7805
310	6974	327	41	2.320	0.276	18.4644	2.8272	22.7805
367	6661	389	28	0.604	0.976	35.3886	10.9614	22.0741
433	7311	449	63	2.309	1.626	32.3243	13.6394	22.1725
459	6426	484	27	0.239	0.299	103.8306	1.3586	20.9055
465	7281	482	67	0.516	0.482	238.9271	66.0013	20.0006
469	6425	497	27	0.657	0.817	76.4266	1.3586	21.2382
477	7027	508	46	0.832	0.784	40.3515	5.6057	21.9317
482	7350	502	64	0.168	0.122	23.3831	0.9858	22.524
504	7280	532	66	2.086	5.548	45.9083	1.4586	21.7916
616	7431	661	70	0.543	2.673	11.0656	2.4387	23.3364
616	7431	661	70	2.760	2.673	11.0656	2.4387	23.3364
623	6935	657	82	1.135	1.048	70.4175	4.5958	21.3271
626	6936	706	82	1.752	0.434	28.1772	4.5958	22.3216
643	6432	702	23	1.003	1.181	56.2574	1.0000	21.5709
655	6936	712	82	1.882	0.434	15.3223	4.5958	22.983
656	7061	707	74	1.650	1.444	38.0859	4.0735	21.9944
671	6432	724	23	1.239	1.181	17.9575	1.0000	22.8107
692	6966	755	83	0.305	0.311	20.9424	4.5965	22.6437

Continued on next page

Table 5 – continued from previous page

Grism ID	NCS ID	SE ID	Merger ID	z_{grism}	z_{phot}	F160W Flux	Merger Flux Ratio	F160W Magnitude
713	7255	774	77	0.001	0.038	316.8257	8.9862	19.6943
723	6596	748	15	1.032	1.018	66.5200	nan	21.3889
725	7085	736	75	0.914	0.636	105.4524	22.8355	20.8887
734	7213	799	73	2.355	0.527	631.0433	1.1031	18.9462
734	7213	800	73	2.355	0.527	696.0784	1.1031	18.8397
736	6372	1295	21	2.000	1.698	58.7216	1.4828	21.5243
757	6754	1314	24	1.509	0.159	85.6159	4.0003	21.1149
775	6608	1238	11	0.828	0.822	225.4820	nan	20.0635
789	7252	904	96	2.087	3.305	527.1860	1.1376	19.1414
813	6983	973	100	0.537	0.691	156.9164	27.5985	20.4571
827	6402	949	6	0.378	0.447	13.7645	3.4264	23.0994
832	6402	936	6	0.402	0.447	14.2825	3.4264	23.0593
832	6402	936	6	0.360	0.447	14.2825	3.4264	23.0593
840	6951	1380	104	2.231	2.005	77.6274	0.3493	21.2213
875	6851	1010	20	1.935	0.451	54.2616	7.7613	21.6101
887	6455	1000	5	0.273	0.231	407.3409	4.6891	19.4214
961	7170	1097	91	0.834	0.671	284.0117	20.5060	19.813
978	6744	1125	17	1.181	3.055	15.0012	6.7166	23.006
978	6744	1125	17	2.840	3.055	15.0012	6.7166	23.006
1027	6581	1153	10	1.289	0.747	22.3704	7.3547	22.5721

Continued on next page

Table 5 – continued from previous page

Grism ID	NCS ID	SE ID	Merger ID	z_{grism}	z_{phot}	F160W Flux	Merger Flux Ratio	F160W Magnitude
1059	6516	1175	12	0.822	0.784	36.5473	1.2629	22.0392
1088	6535	1166	14	0.614	2.785	9.1053	2.6842	23.5481
1088	6535	1166	14	0.829	2.785	9.1053	2.6842	23.5481
1103	7043	1156	76	0.763	0.128	32.0079	1.5389	22.1832
1130	6971	1131	85	0.799	0.844	60.8593	nan	21.4855
1140	6535	1221	14	0.407	2.785	8.1353	2.6842	23.6704
1140	6535	1221	14	0.859	2.785	8.1353	2.6842	23.6704
1206	6896	1443	101	2.029	1.330	100.1680	10.6032	20.9445
1261	6521	881	5	1.236	1.227	86.8703	4.6891	21.0991
1263	6959	1478	102	2.722	1.415	27.6304	4.4643	22.3428
1285	6760	1046	3	1.141	1.330	42.3250	10.6246	21.8798
1288	6958	985	102	2.734	1.587	123.3492	4.4643	20.7185

Table 6: IRC0222B Merger Coordinate Data

Grism ID	NCS ID	SE ID	NCS RA	NCS DEC	HST RA	HST DEC	DQ	Q_z
17	7368	1	35.5817	-4.3791	35.5816	-4.3791	1	1
57	7342	30	35.5847	-4.3770	35.5848	-4.3771	1	3
65	7388	3	35.5838	-4.3781	35.5837	-4.3781	1	3

Continued on next page

Table 6 – continued from previous page

Grism ID	NCS ID	SE ID	NCS RA	NCS DEC	HST RA	HST DEC	DQ	Q_z
84	6826	75	35.5892	-4.3598	35.5891	-4.3598	1	3
98	7392	92	35.5827	-4.3781	35.5826	-4.3781	1	0
103	7367	112	35.5811	-4.3783	35.5811	-4.3783	1	1
157	7259	159	35.5815	-4.3744	35.5814	-4.3744	1	3
167	7306	171	35.5811	-4.3761	35.5810	-4.3761	1	3
179	6546	189	35.5893	-4.3519	35.5892	-4.3519	1	3
185	7305	192	35.5811	-4.3754	35.5811	-4.3753	1	2
185	7305	192	35.5811	-4.3754	35.5811	-4.3753	1	1
187	6947	208	35.5848	-4.3619	35.5847	-4.3619	1	2
206	6880	217	35.5834	-4.3617	35.5833	-4.3617	1	3
217	6772	225	35.5860	-4.3584	35.5860	-4.3583	1	3
223	6536	236	35.5884	-4.3517	35.5884	-4.3517	1	1
247	6841	253	35.5839	-4.3603	35.5838	-4.3601	1	3
256	6694	267	35.5854	-4.3560	35.5854	-4.3560	1	1
277	6866	292	35.5835	-4.3610	35.5834	-4.3610	1	3
277	6866	292	35.5835	-4.3610	35.5834	-4.3610	1	3
297	6712	318	35.5836	-4.3568	35.5835	-4.3568	1	3
310	6974	327	35.5811	-4.3653	35.5810	-4.3654	1	2
310	6974	327	35.5811	-4.3653	35.5810	-4.3654	1	3
367	6661	389	35.5816	-4.3558	35.5816	-4.3560	1	1
433	7311	449	35.5735	-4.3761	35.5735	-4.3761	1	1
459	6426	484	35.5827	-4.3488	35.5827	-4.3488	1	1

Continued on next page

Table 6 – continued from previous page

Grism ID	NCS ID	SE ID	NCS RA	NCS DEC	HST RA	HST DEC	DQ	Q_z
465	7281	482	35.5716	-4.3752	35.5715	-4.3752	1	3
469	6425	497	35.5820	-4.3488	35.5819	-4.3488	1	3
477	7027	508	35.5760	-4.3669	35.5760	-4.3670	1	3
482	7350	502	35.5729	-4.3772	35.5728	-4.3773	0	0
504	7280	532	35.5709	-4.3777	35.5708	-4.3778	0	0
616	7431	661	35.5676	-4.3804	35.5675	-4.3804	0	0
616	7431	661	35.5676	-4.3804	35.5675	-4.3804	0	0
623	6935	657	35.5716	-4.3639	35.5716	-4.3639	1	3
626	6936	706	35.5719	-4.3646	35.5718	-4.3647	1	1
643	6432	702	35.5774	-4.3485	35.5772	-4.3484	1	3
655	6936	712	35.5719	-4.3646	35.5721	-4.3646	1	1
656	7061	707	35.5710	-4.3680	35.5709	-4.3680	1	2
671	6432	724	35.5774	-4.3485	35.5775	-4.3486	0	0
692	6966	755	35.5712	-4.3655	35.5710	-4.3653	1	1
713	7255	774	35.5641	-4.3743	35.5640	-4.3743	1	1
723	6596	748	35.5722	-4.3536	35.5721	-4.3535	1	3
725	7085	736	35.5673	-4.3690	35.5672	-4.3690	1	3
734	7213	799	35.5672	-4.3730	35.5670	-4.3727	0	0
734	7213	800	35.5672	-4.3730	35.5673	-4.3732	0	0
736	6372	1295	35.5743	-4.3469	35.5742	-4.3470	0	0
757	6754	1314	35.5707	-4.3582	35.5706	-4.3582	1	3
775	6608	1238	35.5699	-4.3542	35.5699	-4.3543	1	3

Continued on next page

Table 6 – continued from previous page

Grism ID	NCS ID	SE ID	NCS RA	NCS DEC	HST RA	HST DEC	DQ	Q_z
789	7252	904	35.5558	-4.3742	35.5559	-4.3739	0	0
813	6983	973	35.5589	-4.3659	35.5588	-4.3659	1	2
827	6402	949	35.5653	-4.3474	35.5653	-4.3473	1	2
832	6402	936	35.5653	-4.3474	35.5652	-4.3474	1	3
832	6402	936	35.5653	-4.3474	35.5652	-4.3474	1	3
840	6951	1380	35.5549	-4.3649	35.5548	-4.3650	1	2
875	6851	1010	35.5624	-4.3605	35.5623	-4.3606	0	0
887	6455	1000	35.5626	-4.3496	35.5626	-4.3497	1	2
961	7170	1097	35.5607	-4.3714	35.5606	-4.3714	0	0
978	6744	1125	35.5657	-4.3577	35.5656	-4.3577	1	3
978	6744	1125	35.5657	-4.3577	35.5656	-4.3577	1	3
1027	6581	1153	35.5685	-4.3528	35.5686	-4.3529	1	3
1059	6516	1175	35.5703	-4.3513	35.5703	-4.3514	1	3
1088	6535	1166	35.5719	-4.3519	35.5718	-4.3520	0	0
1088	6535	1166	35.5719	-4.3519	35.5718	-4.3520	1	3
1103	7043	1156	35.5666	-4.3675	35.5665	-4.3677	1	1
1130	6971	1131	35.5673	-4.3653	35.5673	-4.3653	1	2
1140	6535	1221	35.5719	-4.3519	35.5718	-4.3518	0	0
1140	6535	1221	35.5719	-4.3519	35.5718	-4.3518	1	2
1206	6896	1443	35.5592	-4.3629	35.5592	-4.3630	1	3
1261	6521	881	35.5635	-4.3494	35.5635	-4.3494	1	2
1263	6959	1478	35.5574	-4.3649	35.5573	-4.3650	1	1

Continued on next page

Table 6 – continued from previous page

Grism ID	NCS ID	SE ID	NCS RA	NCS DEC	HST RA	HST DEC	DQ	Q_z
1285	6760	1046	35.5586	-4.3580	35.5585	-4.3581	1	1
1288	6958	985	35.5568	-4.3649	35.5567	-4.3649	1	1